

A hybrid transient CFD-thermoelectric numerical model for automobile thermoelectric generator systems

Ding Luo^{a,**}, Yuying Yan^b, Ying Li^b, Ruochen Wang^d, Lulu Zhang^a, Hao Chen^c, Xuelin Yang^{a,*}

^a College of Materials and Chemical Engineering, Hubei Provincial Collaborative Innovation Center for New Energy Microgrid, China Three Gorges University, Yichang, China

^b Faculty of Engineering, University of Nottingham, Nottingham, UK

^c Shaanxi Key Laboratory of New Transportation Energy and Automotive Energy Saving, Chang'an University, Xi'an, China

^d School of Automobile and Traffic Engineering, Jiangsu University, Zhenjiang, China

Corresponding authors: *Xuelin Yang, xlyang@ctgu.edu.cn; **Ding Luo, Ding_L@outlook.com;

Abstract: Dynamic performance prediction of the automobile thermoelectric generator system is one of the research hotspots in the field of thermoelectric technology. In this work, a hybrid transient CFD-thermoelectric numerical model is proposed for the first time to predict the dynamic response characteristics of an automobile thermoelectric generator system. Taking the exhaust gas of a heavy truck under a highway fuel economy test driving cycle as the transient heat source, the transient numerical study on the automobile thermoelectric generator system is carried out. It is found that the dynamic output power of the automobile thermoelectric generator system changes more smoothly than exhaust temperature due to the effect of thermal inertia, while the conversion efficiency fluctuates greatly. The transient output power at $t = 467$ s and transient conversion efficiency at $t = 635$ s reach the highest values at 45.16 W and 39.68%, respectively. Within the period of 765 s, the total power generation and average conversion efficiency of the automobile thermoelectric generator system are 26460 J and 3.29%, respectively. Through the transient experimental validation, the average error of transient output voltage between experimental and model results is 6.43%. This work fills the gap in the dynamic performance prediction of thermoelectric devices used for fluid waste heat recovery. The findings are helpful in better understanding the dynamic response characteristics of the automobile thermoelectric generator system.

Keywords: dynamic performance; numerical model; thermoelectric; thermoelectric generator system; exhaust gas; dynamic response.

Nomenclature			
<i>Symbols</i>		ϕ	electrical potential, V
A	area, m ²	α	Seebeck coefficient, $\mu\text{V}\cdot\text{K}^{-1}$
c	specific heat, $\text{J}\cdot\text{kg}^{-1}\cdot\text{K}^{-1}$	η	conversion efficiency
\vec{E}	electric field density vector, $\text{V}\cdot\text{m}^{-2}$	<i>Subscripts</i>	
I	output current, A	c	cold side
\vec{j}	current density vector, $\text{A}\cdot\text{m}^{-2}$	co	copper
k	turbulent kinetic energy, $\text{m}^2\cdot\text{s}^{-2}$	ex	exhaust gas
\dot{m}	mass flow rate, $\text{g}\cdot\text{s}^{-1}$	exi	exhaust inlet
p	pressure, Pa	exo	exhaust outlet
P	output power, W	h	hot side
Q	heat absorption, W	i	i=1, 2, 3, and 4
R	resistance, Ω or K/W	L	load resistance
\dot{S}	source term	m	material name
t	time, s	n	n-type thermoelectric semiconductor
T	temperature, K	out	outlet surface
U	output voltage, V	p	p-type thermoelectric semiconductor
\vec{v}	velocity, $\text{m}\cdot\text{s}^{-1}$	<i>Abbreviations</i>	
<i>Greek symbols</i>		CFD	computational fluid dynamics
λ	thermal conductivity, $\text{W}\cdot\text{m}^{-1}\cdot\text{K}^{-1}$	EUDC	extra urban driving cycle
ρ	density, $\text{kg}\cdot\text{m}^{-3}$	FEM	finite element method
μ	dynamic viscosity, $\text{Pa}\cdot\text{s}$	FVM	finite volume method
ε	turbulent dissipation rate, $\text{m}^2\cdot\text{s}^{-3}$	LHDC	long haulage driving cycle
σ	electrical conductivity, $\text{S}\cdot\text{m}^{-1}$	TEG	thermoelectric generator
σ^{-1}	electrical resistivity, $\Omega\cdot\text{m}$	TEM	thermoelectric module
		HWFET	highway fuel economy test

1. Introduction

For engine-powered vehicles, the waste heat contained in automobile exhaust gas accounts for about one-third of the total energy generated by burning fossil fuels and is directly discharged into the environment [1], resulting in serious energy waste and environmental pollution. Recycling this waste heat is one of the effective ways to improve engine thermal efficiency and reduce fuel consumption. Thermoelectric power generation is considered to be a promising technology, which can directly convert exhaust heat into electricity and improve the fuel economy of vehicles [2]. It was reported that the automobile thermoelectric generator (TEG) system has the potential to save 6% of fuel consumption [3]. In recent years, a great number of automobile TEG systems have been reported in the literature, which can produce a maximum output power of tens of watts to kilowatts, as listed in Table 1. The power generation of the mentioned automobile TEG systems was obtained by

experimental measurements or theoretical models. As is well known, the theoretical model is necessary to guide the design and optimization of automobile TEG systems. Therefore, the development of a reasonable model for the automobile TEG system has become the focus of researchers [4].

Table 1. Automobile thermoelectric generator systems in published literature.

Vehicle or engine type	Number of TEG modules	Working conditions	Steady-state or transient state	Experimental test or model prediction	Generated power	Ref
BMW X6	-	US06 driving cycle	transient state	experimental test	from 0 to ~500 W	[5]
Lincoln MKT	-	highway driving cycle	transient state	experimental test	from ~50 W to ~300 W	[5]
heavy-duty diesel engine	20	non-road transient cycle	transient state	model prediction	from 0 W to ~300 W	[6]
off-road vehicle	240	engine power: 51 kW	steady-state	experimental test	maximum power: 944 W	[7]
gasoline engine	12	EUDC driving cycle	transient state	experimental test	from ~2 W to ~30 W	[8]
heavy-duty vehicle	240	LHDC driving cycle	transient state	experimental test	from ~300 W to ~820 W	[9]
gasoline engine	306	engine power: 30.4 kW	steady-state	model prediction	maximum power: 515 W	[10]

* Extra Urban Driving Cycle (EUDC); ** long haulage driving cycle (LHDC)

The existing theoretical models for predicting the performance of the automobile TEG system can be classified into two categories: the analytical model [11] and the numerical model [12]. The analytical model is deduced by analyzing the heat transfer process from the exhaust gas to the heat exchanger, thermoelectric module (TEM) arrays, heat sinks, and finally to coolant, which can quickly calculate the output performance under the given temperature and mass flow rate, but can not consider the factors such as heat loss, temperature distribution, and complex geometry. The analytical model has been proved to be unreasonable compared with the numerical model [13]. Especially in recent years, with the development of numerical analysis software, more and more researchers use numerical models based on the finite element method (FEM) [14] or finite volume method (FVM) [15] to predict the performance of TEGs and TEG systems. Furthermore, the numerical models for the automobile TEG system include: (i) computational fluid dynamics (CFD) model, which can analyze the thermal and pressure performance of the automobile TEG system without considering the thermal-electric coupling effects [16]; (ii) thermal-electric numerical model, which can analyze the thermoelectric performance of the system by simplifying the heat transfer from the exhaust gas to TEM arrays [17]; and (iii) recently reported fluid-thermal-electric numerical model, which can comprehensively evaluate the output performance of the system through some geometric simplifications [18].

However, most of the models reported at present are steady-state, which is not consistent with the actual vehicle conditions. Steady-state models can not meet the needs of dynamic performance prediction of the automobile TEG system under actual driving conditions. Also, it was reported that the power generation of the automobile TEG system under a complete driving cycle is lower than that

expected from a steady-state analysis [8]. To obtain more accurate analysis results, it is necessary to extend the model from steady-state to transient state. There are three routes to develop the transient theoretical models: transient analytical model, transient numerical model, and hybrid transient model.

Firstly, the analytical model has the advantages of no consumption of computing resources and simple modeling. In the previous studies [19-21], some steady-state analytical models for automobile TEG systems have been established, which can consider the temperature dependence of thermoelectric materials and heat loss. However, the developed models can not be used to predict dynamic performance. By introducing a time variable into the equations of the steady-state analytical model, Lan et al. [6] proposed a transient analytical model to estimate the dynamic output performance of an automobile TEG system. The discrete data of exhaust temperature and mass flow rate under the New European Driving Cycle (NEDC) were imported into the dynamic model, and the output parameters at corresponding time points were calculated. Nevertheless, the transient analytical model features the major drawback that the thermal inertia can not be considered, which further increases the error of the analytical model itself.

Secondly, the numerical model can simulate the actual working conditions of the automobile TEG system and predict its performance with high accuracy, but it has the disadvantage of long computation time. The steady-state CFD model [22] is the most widely used model to analyze the thermal-hydraulic performance of automobile TEG systems. Kempf and Zhang [23] first optimized the parameters of the heat exchanger via the steady-state CFD model and then designed a 1-kW automobile TEG system prototype based on CFD results [24]. However, there is no report about transient CFD modeling for the automobile TEG system. Different from the CFD model, the thermal-electric numerical model has made great progress. From 2D [25] to 3D [14], from steady-state [26] to transient state [27], a large number of thermal-electric numerical models have been used to evaluate the performance of TEGs. The thermal-electric numerical model suffers from the main limitation that the fluid flow of exhaust gas and cooling water can not be considered. To address this issue, Ma et al. [28] and Yan et al. [18] proposed a 3D steady-state fluid-thermal-electric multiphysics numerical model of the automobile TEG system by integrating a thermal-electric numerical model into CFD model. In their studies, the TEM was simplified into a thermoelectric couple [28], and the geometry of heat sinks was ignored [18]. The fluid-thermal-electric multiphysics numerical model takes into account the coupling effects of fluid, thermal, and electric fields. Even though it needs huge computing time and resources, extending it from the simplified geometry to the whole structure, from steady-state to transient state is the best way to predict the transient performance of automobile TEG systems. However, it still requires

tremendous studies.

Thirdly, another effective way to develop a transient model for automobile TEG systems is to combine different models to form a hybrid model and extend it from steady-state to transient state. Li et al. [29] used the temperature data from steady-state CFD simulation as the boundary conditions of the analytical model of TEMs, and then worked out the output performance of the automobile TEG system. The model makes full use of the advantages of the CFD model and the analytical model, but it inevitably has the limitations of the analytical model. Furthermore, Luo et al. [30] proposed a steady-state hybrid numerical model for an air-to-water TEG system by combining the thermal-electric numerical model with the CFD model. In the following work [31], the authors extended the model from a TEG system with one TEM to a TEG system with a series of TEMs. The proposed hybrid steady-state numerical model was experimentally verified, which provides a new approach to evaluating the performance of automobile TEG systems. Comparing the abovementioned methods of extending these two hybrid models from steady-state to transient state, the latter one is a more attractive one, because the analytical model in the first model can not consider the thermal inertia, which further increases its own error. The hybrid transient CFD-thermoelectric numerical model can not only maintain a high accuracy of the numerical models but also reduce the computational complexity and time, which is the key point of this work.

Table 2 summarizes the latest development of theoretical models for automobile TEG systems. It can be noticed that there are few reports on the transient theoretical model. However, due to the overestimation of performance in steady-state analysis, it is necessary to study the dynamic performance of the automobile TEG system. Although the fluid-thermal-electric numerical model features ultrahigh precision and reasonability, the existing steady-state model has a large number of geometric simplifications. Besides, the fluid-thermal-electric numerical model needs plenty of computing time and resources, and it suffers from convergence problems during the numerical calculation. Therefore, the hybrid CFD-thermoelectric numerical model is an attractive choice to develop its transient model. Compared with the fluid-thermal-electric numerical model, the hybrid CFD-thermoelectric numerical model can significantly shorten the execution time, because the CFD model and the thermal-electric numerical model are solved separately at the same time. The only drawback of the hybrid CFD-thermoelectric numerical model is that it can not consider the influence of heat generated by TEMs on the CFD model. However, compared with the heat contained in the exhaust gas, the heat generated by TEMs is tiny and can be ignored. Therefore, this assumption will not seriously affect the predicted output performance. More importantly, the validity of the hybrid

CFD-thermoelectric numerical model in steady-state has already been verified by experiments in previous studies [31, 32].

Table 2. Recent advances of theoretical models for automobile TEG systems

model type		current states	advantages	disadvantages
analytical model		steady-state: [19] transient state: [6, 33]	<ul style="list-style-type: none"> • rapid computation • convenience for modeling 	<ul style="list-style-type: none"> • rough precision • low dimensional • ignoring the thermal inertia
	CFD model	steady-state: [34] transient state: not reported	<ul style="list-style-type: none"> • convenience for studying the thermal-hydraulic performance 	<ul style="list-style-type: none"> • ignoring the thermoelectric coupling effects
numerical models	thermal-electric model	steady state: [35, 36] transient state: [25, 27]	<ul style="list-style-type: none"> • convenience for studying the thermoelectric performance 	<ul style="list-style-type: none"> • ignoring the fluid flow and conjugate heat transfer
	fluid-thermal-electric model	steady-state: [18, 28] transient state: not reported	<ul style="list-style-type: none"> • ultrahigh high precision • potential to fully simulate actual conditions 	<ul style="list-style-type: none"> • huge computing time and resources • many geometric simplifications for the reported models
hybrid models	CFD-analytical model	steady-state: [29] transient state: not reported	<ul style="list-style-type: none"> • relatively short computing time 	<ul style="list-style-type: none"> • ignoring the thermoelectric coupling effects
	CFD-thermoelectric model	steady state: [31, 32] transient state: not reported	<ul style="list-style-type: none"> • relatively short computing time and high precision 	<ul style="list-style-type: none"> • ignoring the effect of heat generated by TEMs on the CFD model

This work serves the purpose of providing a reasonable transient model to evaluate the dynamic response characteristics of the automobile TEG system under actual vehicle transient driving cycles. For this reason, a hybrid transient CFD-thermoelectric numerical model considering transient input of the exhaust heat source, temperature dependence, impedance matching, and heat loss is proposed for the first time. It features the advantages of high accuracy and short calculation time. This study fills the gap in the theoretical prediction of the transient behavior of the automobile TEG system and provides a new perspective for predicting dynamic response characteristics of the automobile TEG system. This paper is structured as follows: Section 2 introduces the hybrid transient CFD-thermoelectric numerical model in detail, including the geometry structure of the automobile TEG system, governing equations, boundary conditions, grid independence analysis, and experimental validation; Section 3 elucidates the results and gives a detailed analysis of the results; Finally, the main research findings are summarized in Section 4.

2. Hybrid transient CFD-thermoelectric numerical model

2.1 Structure of the automobile thermoelectric generator system

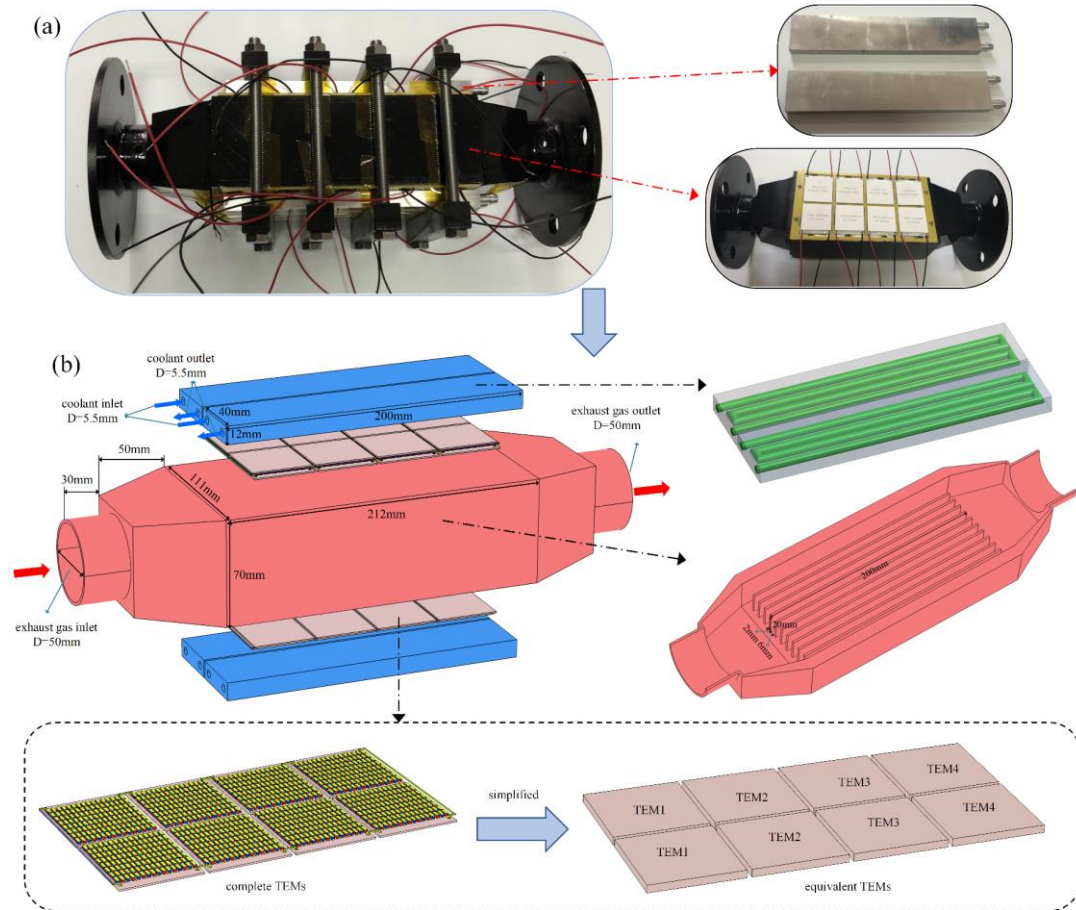


Fig. 1. Architecture of the adopted automobile thermoelectric generator system. (a) The actual prototype of the automobile thermoelectric generator system. (b) Structure diagram of the automobile thermoelectric generator system.

In this work, an automobile thermoelectric generator (TEG) system presented in the previous study [31] is taken as the research objective, and the dynamic response characteristics of the automobile TEG system under a complete transient driving cycle are studied through the proposed hybrid transient computational fluid dynamics (CFD) -thermoelectric numerical model. The structure of the automobile TEG system is shown in Fig. 1, which includes an actual prototype (Fig. 1(a)) and the structure diagram (Fig. 1(b)). The automobile TEG system consists of a heat exchanger, sixteen thermoelectric modules (TEMs), and four heat sinks, which are clamped and fixed by stainless steel bars. Both heat sinks and the heat exchanger are made of 6063 aluminum alloys. Twenty long fins with a size of 20 mm × 2 mm × 200 mm are arranged on the upper and bottom walls of the heat exchanger. High-temperature exhaust gas enters and leaves the heat exchanger through a circular tube with a diameter of 50 mm. The diameter of the coolant channel in the heat sink is 5.5 mm. Detailed geometric features and dimensions can be found in Fig. 1.

Besides, the sixteen TEMs are evenly distributed on the upper and bottom sides of the heat exchanger. The TEM consists of two ceramic plates, 256 copper sheets, 128 pairs of p-type and n-type

thermoelectric legs. The dimensions of the hot-side ceramic plate, copper sheets, thermoelectric legs, and cold-side ceramic plate are 44 mm × 40 mm × 0.8 mm, 3.8 mm × 1.4 mm × 0.35 mm, 1.4 mm × 1.4 mm × 1 mm, and 40 mm × 40 mm × 0.8 mm, respectively. During transient CFD numerical simulations, to shorten the calculation time, the complete TEM is simplified to a cube with an equivalent size of 40 mm × 40 mm × 3.3 mm. According to the CFD results, the average surface temperatures on both sides of TEMs are obtained, which are used as the temperature boundary conditions of the transient thermal-electric numerical model. During transient thermal-electric numerical simulations, the complete TEM structure is adopted. A load resistance is connected in series with the four TEMs. Detailed properties of the materials in the automobile TEG system are listed in Table 3. Here, the thermal conductivity of the equivalent TEM is obtained according to the reported method in [20], where the contact thermal resistance inside the TEM has already been considered in the experimental measurement process. As for the contact thermal resistances between the TEM and heat exchangers, they are ignored due to the use of clamping devices and thermal extensional structures [37, 38]. The material properties of exhaust gas and coolant are not given, because they are replaced by dry air and water, respectively. The properties of air and water are from the material library of COMSOL Multiphysics [39], and the temperature-dependent properties of the thermoelectric materials are taken into account.

Table 3. Material parameters of the automobile TEG system.

Material	Components	Parameter name	Value	Unit	
p-type thermoelectric material	p-type legs	thermoelectric	Seebeck coefficient	$-1.80268 \times 10^{-7} T^4 + 3.23632 \times 10^{-4} T^3 - 0.21537 T^2 + 62.97444 T - 6616.56781$	$\text{W} \cdot \text{m}^{-1} \cdot \text{K}^{-1}$
			electrical resistivity	$-3.08802 \times 10^{-9} T^4 + 4.56531 \times 10^{-6} T^3 - 2.58541 \times 10^{-3} T^2 + 0.65579 T - 60.58804$	$10^{-5} \text{ohm} \cdot \text{m}$
		thermoelectric	thermal conductivity	$-3.05948 \times 10^{-9} T^4 + 4.56781 \times 10^{-6} T^3 - 2.51621 \times 10^{-3} T^2 + 0.61074 T - 53.98632$	$\mu\text{V} \cdot \text{K}^{-1}$
			density	6600	$\text{kg} \cdot \text{m}^{-3}$
		thermoelectric	specific heat	188	$\text{J} \cdot \text{kg}^{-1} \cdot \text{K}^{-1}$
			Seebeck coefficient	$1.80268 \times 10^{-7} T^4 - 3.23632 \times 10^{-4} T^3 + 0.21537 T^2 - 62.97444 T + 6616.56781$	$\text{W} \cdot \text{m}^{-1} \cdot \text{K}^{-1}$
n-type thermoelectric material	n-type legs	thermoelectric	Seebeck coefficient	$1.80268 \times 10^{-7} T^4 - 3.23632 \times 10^{-4} T^3 + 0.21537 T^2 - 62.97444 T + 6616.56781$	$\text{W} \cdot \text{m}^{-1} \cdot \text{K}^{-1}$
			electrical resistivity	$-3.08802 \times 10^{-9} T^4 + 4.56531 \times 10^{-6} T^3 - 2.58541 \times 10^{-3} T^2 + 0.65579 T - 60.58804$	$10^{-5} \text{ohm} \cdot \text{m}$
		thermoelectric	thermal conductivity	$-3.05948 \times 10^{-9} T^4 + 4.56781 \times 10^{-6} T^3 - 2.51621 \times 10^{-3} T^2 + 0.61074 T - 53.98632$	$\mu\text{V} \cdot \text{K}^{-1}$
			density	6600	$\text{kg} \cdot \text{m}^{-3}$
		thermoelectric	specific heat	188	$\text{J} \cdot \text{kg}^{-1} \cdot \text{K}^{-1}$
			Seebeck coefficient	$1.80268 \times 10^{-7} T^4 - 3.23632 \times 10^{-4} T^3 + 0.21537 T^2 - 62.97444 T + 6616.56781$	$\text{W} \cdot \text{m}^{-1} \cdot \text{K}^{-1}$
copper	copper sheets	thermoelectric	electrical resistivity	1.75×10^{-8}	$\text{ohm} \cdot \text{m}$
			thermal conductivity	165.64	$\text{W} \cdot \text{m}^{-1} \cdot \text{K}^{-1}$
		thermoelectric	density	8978	$\text{kg} \cdot \text{m}^{-3}$
			specific heat	381	$\text{J} \cdot \text{kg}^{-1} \cdot \text{K}^{-1}$
			Seebeck coefficient	$1.80268 \times 10^{-7} T^4 - 3.23632 \times 10^{-4} T^3 + 0.21537 T^2 - 62.97444 T + 6616.56781$	$\text{W} \cdot \text{m}^{-1} \cdot \text{K}^{-1}$
-	load resistance	thermoelectric	electrical resistance	17	ohm
			thermal conductivity	165.64	$\text{W} \cdot \text{m}^{-1} \cdot \text{K}^{-1}$

		density	8978	$\text{kg}\cdot\text{m}^{-3}$
		specific heat	381	$\text{J}\cdot\text{kg}^{-1}\cdot\text{K}^{-1}$
ceramic	ceramic plates	thermal conductivity	22	$\text{W}\cdot\text{m}^{-1}\cdot\text{K}^{-1}$
		density	3600	$\text{kg}\cdot\text{m}^{-3}$
		specific heat	850	$\text{J}\cdot\text{kg}^{-1}\cdot\text{K}^{-1}$
6063 aluminum alloys	heat exchanger and heat sinks	thermal conductivity	201	$\text{W}\cdot\text{m}^{-1}\cdot\text{K}^{-1}$
		density	2719	$\text{kg}\cdot\text{m}^{-3}$
		specific heat	871	$\text{J}\cdot\text{kg}^{-1}\cdot\text{K}^{-1}$
-	equivalent TEM	thermal conductivity	$-2.90574\times 10^{-9}T^4 + 4.33411\times 10^{-6}T^3 - 0.00239T^2 + 0.57868T - 51.05908$	$\text{W}\cdot\text{m}^{-1}\cdot\text{K}^{-1}$
		density	6600	$\text{kg}\cdot\text{m}^{-3}$
		specific heat	188	$\text{J}\cdot\text{kg}^{-1}\cdot\text{K}^{-1}$

2.2 Governing equations of the hybrid transient CFD-thermoelectric numerical model

The hybrid transient CFD-thermoelectric numerical model consists of two sub-models: a transient CFD model and a transient thermal-electric numerical model. During the complete numerical calculation process, the transient CFD model is firstly solved, and then the transient thermal-electric numerical model is solved. The average surface temperatures on both sides of TEMs obtained by the transient CFD model are used as temperature boundary conditions of the transient thermal-electric numerical model. For the transient CFD model, the transient mass, momentum, and temperature conservation equations [40] can be expressed as follows:

$$\frac{\partial \rho}{\partial t} + \nabla \cdot (\rho \vec{v}) = 0 \quad (1)$$

$$\frac{\partial}{\partial t} (\rho \vec{v}) + \nabla \cdot (\rho \vec{v} \vec{v}) = -\nabla p + \nabla \cdot [\mu (\nabla \vec{v} + \nabla \vec{v}^T)] \quad (2)$$

$$\rho c \frac{\partial T}{\partial t} + \rho c \vec{v} \cdot \nabla T - \nabla \cdot (\lambda \nabla T) = 0 \quad (3)$$

where ρ , t , \vec{v} , p , μ , c , T , and λ represent the density, time, velocity, pressure, dynamic viscosity, specific heat at constant pressure, temperature, and thermal conductivity of fluids, respectively.

In general, the fluid flow of exhaust gas in the heat exchanger and that of coolant in heat sinks are turbulent and can be considered incompressible. The standard $k - \varepsilon$ turbulence model [40] is adopted to compute the turbulent flow in the current research, and the transport equations for k and ε are:

$$\frac{\partial}{\partial t} (\rho k) + \rho (\vec{v} \cdot \nabla) k = \nabla \cdot \left[\left(\mu + \frac{\mu_t}{\sigma_k} \right) \nabla k \right] + P_k - \rho \varepsilon \quad (4)$$

$$\frac{\partial}{\partial t} (\rho \varepsilon) + \rho (\vec{v} \cdot \nabla) \varepsilon = \nabla \cdot \left[\left(\mu + \frac{\mu_t}{\sigma_\varepsilon} \right) \nabla \varepsilon \right] + C_{1\varepsilon} \frac{\varepsilon}{k} P_k - C_{2\varepsilon} \rho \frac{\varepsilon^2}{k} \quad (5)$$

with

$$\mu_t = \rho C_\mu \frac{k^2}{\varepsilon} \quad (6)$$

where k , ε , and P_k are the turbulence kinetic energy, dissipation of turbulence kinetic energy, and shear production of turbulence kinetic energy, respectively. $C_{1\varepsilon} = 1.44$, $C_{2\varepsilon} = 1.92$, $C_\mu = 0.09$, $\sigma_k = 1.0$, and $\sigma_\varepsilon = 1.3$ [41] are model constants.

The governing equations of the fluid are given by Eqs. (1)-(6). For the solid region in the CFD model, to calculate the heat transfer of the thermal field, the transient energy conservation is defined as:

$$(\rho c)_m \frac{\partial T}{\partial t} = \nabla \cdot (\lambda_m \nabla T) \quad (7)$$

where subscript m denotes different materials.

The above equations constitute the governing equations of the transient CFD model. The transient CFD model can be used to analyze the transient thermodynamic performance of the automobile TEG system. However, the transient response of the electric field of the automobile TEG system can not be obtained by the transient CFD model. In this work, the transient thermal-electric numerical model is used to calculate the electrical output performance of the automobile TEG system.

The governing equations of the transient thermal-electric numerical model include the energy conservation equation, electric field conservation equation, and current continuity equation. Here, the energy conservation of the transient thermal-electric numerical model is expressed as [27]:

$$(\rho c)_m \frac{\partial T}{\partial t} = \nabla \cdot (\lambda_m \nabla T) + \dot{S}_m \quad (8)$$

with

$$\dot{S}_m = \begin{cases} \sigma_p^{-1}(T) \vec{J}^2 - \nabla \alpha_p(T) \vec{J} T_p; & \text{p-type thermoelectric leg} & (9-1) \\ \sigma_n^{-1}(T) \vec{J}^2 - \nabla \alpha_n(T) \vec{J} T_n; & \text{n-type thermoelectric leg} & (9-2) \\ \sigma_{co}^{-1} \vec{J}^2; & \text{copper sheet} & (9-3) \\ \sigma_L^{-1} \vec{J}^2; & \text{load resistance} & (9-4) \\ 0; & \text{ceramic} & (9-5) \end{cases}$$

where, \dot{S}_m denotes the energy source term, which is induced by the electric field. σ^{-1} , α , and \vec{J} are the electrical resistivity, Seebeck coefficient, and current density vector, respectively. Subscripts p, n, co, and L represent the p-type thermoelectric leg, n-type thermoelectric leg, copper sheet, and load resistance, respectively. The first term on the right side of Eqs (9-1) and (9-2) represent Joule heat, and the second term represents Thomson heat along thermoelectric legs or Peltier heat on both ends of thermoelectric legs.

Compared with Eq. (8), the energy source term is absent in Eq. (7), because the electric field is

ignored in the transient CFD model.

The electric field conservation equation of the transient thermal-electric numerical model can be written as [42]:

$$\vec{E} = -\nabla\phi + \alpha_{p,n}(T)\nabla T \quad (10)$$

where \vec{E} and ϕ are the electric field density vector and electrical potential, respectively.

Besides, the current flows through the p-type and n-type thermoelectric legs, copper sheet, and load resistance is continuous, which can be defined as [43]:

$$\nabla \cdot \vec{J} = 0 \quad (11)$$

with

$$\vec{J} = \sigma_m \vec{E} \quad (12)$$

Eqs. (8)-(12) constitute the governing equations of the transient thermal-electric numerical model. To solve the partial differential conservation equations of the transient CFD model and the transient thermal-electric numerical model, the numerical calculation method is essential. The finite element method, finite volume method, and finite difference method are commonly used to solve numerical models. In the present work, the backward difference method and the finite element method are used to discretize the time and space variables, respectively, by the commercial numerical software package of COMSOL.

2.3 Boundary conditions of the hybrid transient CFD-thermoelectric numerical model

Boundary conditions are essential for solving the governing equations of the hybrid transient CFD-thermoelectric numerical model. There are two kinds of boundary conditions: the boundary conditions of the transient CFD model and the boundary conditions of the transient thermal-electric numerical model. Considering the huge computing time and resources required for transient numerical calculation, this study only takes 1/4 of the automobile TEG system as the research objective due to its completely symmetrical structure.

In practice, exhaust parameters are time-dependent and related to vehicle driving conditions. Consequently, the transient inlet boundary conditions of exhaust gas in the transient CFD model, including the transient inlet temperature and mass flow rate of the exhaust gas, are defined. However, other boundary conditions, such as coolant inlet, exhaust outlet, coolant outlet, heat loss, and symmetrical surface, are steady-state. To obtain accurate transient exhaust temperature and mass flow rate, the operating conditions of the heavy truck were simulated by the vehicle simulation software package of ADVISOR [44]. On the platform of ADVISOR, the vehicle type was defined as a heavy truck; the vehicle weight and cargo weight were set at 7068 kg and 2000 kg respectively; the heavy

truck was powered by a diesel engine with a displacement of 7.2 L and a maximum power of 206 kW. Besides, the vehicle was set to operate under the Highway Fuel Economy Test (HWFET) driving cycles. For the first several driving cycles, the exhaust temperature increases dramatically from room temperature, and it reaches an equilibrium state at the 10th driving cycle. At this time, the transient temperature ($T_{ex}(t)$) and mass flow rate ($\dot{m}_{ex}(t)$) of the exhaust gas were recorded and used as the inlet boundary conditions of the transient CFD model, as shown in Fig. 2. Here, the period is 765 s for a complete driving cycle. The exhaust mass flow rate was divided by 4 because only a quarter of the automobile TEG system was considered. It can be observed that the exhaust temperature and vehicle speed change with the exhaust mass flow rate. However, the change in exhaust mass flow rate is more severe than those in exhaust temperature and vehicle speed because of the influence of thermal inertia on temperature and mechanical inertia on vehicle speed.

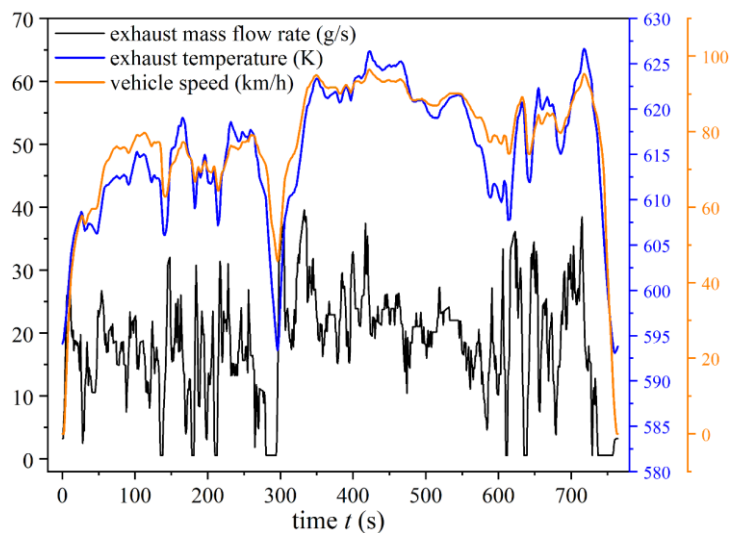


Fig. 2. Transient exhaust temperature and mass flow rate under a complete HWFET driving cycle.

Regarding the steady-state boundary conditions of the transient CFD model, an inlet temperature of 363.15 K and a velocity of 1 m/s are defined as the coolant inlet boundary conditions. Compared with a coolant temperature of room temperature as the inlet boundary condition in other research, the coolant temperature of 363.15 K is more in line with the actual situation. A boundary condition with a standard atmosphere pressure was defined on the outlet surfaces of the exhaust and coolant channels. In this study, exhaust gas and coolant are replaced by dry air and water, respectively. The heat loss boundary condition was defined on the surfaces of the automobile TEG system exposed to the surroundings, of which the ambient temperature is 300 K and the natural convection coefficient is $15 \text{ W}\cdot\text{m}^{-2}\cdot\text{K}^{-1}$. In addition, the symmetric boundary condition was defined on the symmetric surfaces.

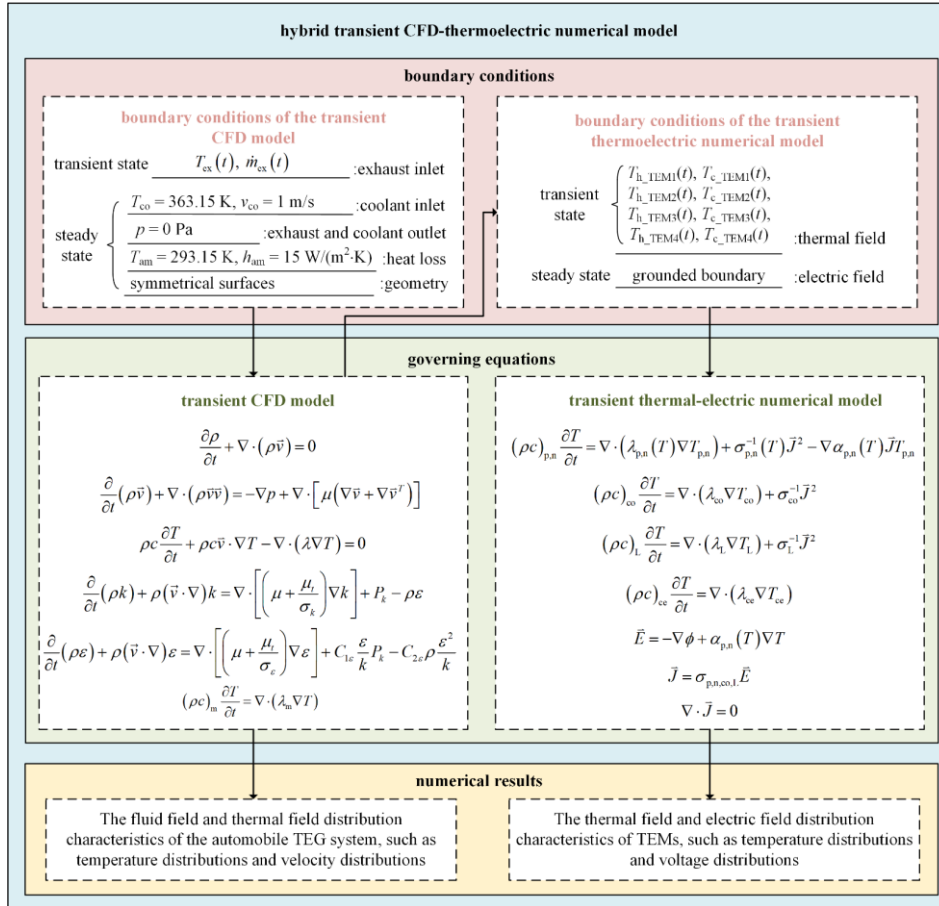


Fig. 3. Relationship between governing equations and boundary conditions of the hybrid transient CFD-thermoelectric numerical model.

As for the transient thermal-electric numerical model, its boundary conditions include transient temperature boundary conditions and steady-state electric field boundary conditions, in which the transient temperature boundary conditions are extracted from the transient CFD results. Based on the CFD results, the transient average temperatures on the hot and cold side surfaces of the equivalent TEMs are obtained, which are taken as the working temperature of the complete TEMs in the transient thermal-electric numerical model. In the quarter structure of the automobile TEG system, the four TEMs are marked as TEM1, TEM2, TEM3, and TEM4 respectively along the direction of the downward flow of the exhaust gas, as can be found in Fig. 1. Two adjacent TEMs are connected in series with copper electrodes, and the load resistance is connected to the remaining terminal of TEM1 and TEM4, as can be seen in Fig. 4(b). In this way, a closed electric circuit is formed. The terminal between TEM4 and load resistance is set to be grounded.

Fig. 3 shows the relationship between the governing equations and boundary conditions of the hybrid transient CFD-thermoelectric numerical model. As can be seen, the transient CFD model of the equivalent automobile TEG system is solved firstly, under the transient boundary conditions of exhaust

gas and other steady-state boundary conditions. Then, the transient hot-side temperatures ($T_{h_TEM1}(t)$, $T_{h_TEM2}(t)$, $T_{h_TEM3}(t)$, and $T_{h_TEM4}(t)$) and transient cold-side temperatures ($T_{c_TEM1}(t)$, $T_{c_TEM2}(t)$, $T_{c_TEM3}(t)$, and $T_{c_TEM4}(t)$) of four TEMs extracted from CFD results are used as transient temperature boundary conditions. Combined with the grounded boundary condition of the transient thermal-electric numerical model, the transient thermal-electric numerical model of the complete TEMs is solved, and the dynamic electric response characteristics of the automobile TEG system are obtained. According to the physical field distribution obtained by the transient CFD model and the dynamic output obtained by the transient thermal-electric numerical model, the transient performance of the automobile TEG system is comprehensively analyzed in the following sections.

2.4 Parameter definitions

Output power and conversion efficiency are the two key parameters to characterize the output performance of the automobile TEG system. Here, the output power of the automobile TEG system is expressed as:

$$P_{out}(t) = \frac{U_L^2(t)}{R_L} \quad (13)$$

where U_L is the output voltage of the four TEMs obtained by the transient thermal-electric numerical model. R_L represents the load resistance. According to the maximum power point in the previous study [31], R_L is set to 17Ω in this work.

Furthermore, the thermal-to-electric conversion efficiency of the automobile TEG system equals the ratio of output power (P_{out}) to heat extracted from exhaust gas (Q_h), that is:

$$\eta(t) = \frac{P_{out}(t)}{Q_h(t)} = \frac{P_{out}(t)}{c_{ex} \dot{m}_{ex}(t) [T_{exi}(t) - T_{exo}(t)]} \quad (14)$$

where, $T_{exi}(t)$ and $T_{exo}(t)$ are the inlet and outlet temperature of the exhaust gas respectively, which are obtained by the transient CFD model.

The output performance of TEMs has an important impact on the overall performance of the automobile TEG system. Also, the TEMs located at different positions produce different outputs due to the uneven temperature distribution. To study the influence of the position of the TEM on its output performance, the output power and conversion efficiency of each TEM are defined as follows:

$$P_{TEMi}(t) = I_L(t) U_{TEMi}(t) = \frac{U_L(t)}{R_L} U_{TEMi}(t) \quad (15)$$

$$\eta_{\text{TEM}_i}(t) = \frac{P_{\text{TEM}_i}(t)}{Q_{\text{TEM}_i}(t)} = \frac{P_{\text{TEM}_i}(t)}{\lambda_{\text{ce}} \frac{A_{\text{h_ce}}}{\delta_{\text{h_ce}}} [T_{\text{h_TEM}_i}(t) - T_{\text{h_cei}}(t)]} \quad (16)$$

where, $P_{\text{TEM}_i}(t)$, $U_{\text{TEM}_i}(t)$, $\eta_{\text{TEM}_i}(t)$, and $Q_{\text{TEM}_i}(t)$ are the output power, output voltage, conversion efficiency, and heat absorption of different TEMs, respectively. $T_{\text{h_cei}}(t)$ is the average temperature of the hot-side ceramic plate of different TEMs on the top surface. The subscript $i = 1, 2, 3$, and 4 denotes the TEM1, TEM2, TEM3, and TEM4 respectively. $I_L(t)$ is the output current. $A_{\text{h_ce}}$ and $\delta_{\text{h_ce}}$ are the cross-sectional area and thickness of the hot-side ceramic plate, respectively. Here, the data of $P_{\text{TEM}_i}(t)$, $U_{\text{TEM}_i}(t)$, $\eta_{\text{TEM}_i}(t)$, $Q_{\text{TEM}_i}(t)$, $T_{\text{h_cei}}(t)$, and $I_L(t)$ are obtained from the transient thermal-electric numerical model.

2.5 Grid analysis

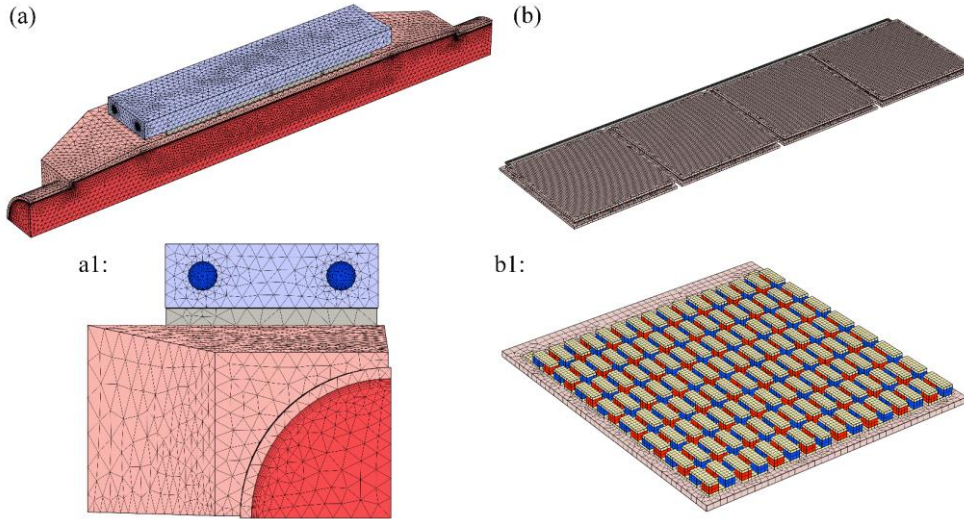


Fig. 4. Finite element model of the automobile TEG system. (a) The equivalent automobile TEG system used for the transient CFD model. (b) The complete TEMs used for the transient thermal-electric numerical model.

The accuracy and computing time of the transient CFD model and transient thermal-electric numerical model are sensitive to the grid parameters of the finite element model. The greater the grid size is, the lower the accuracy and the less the computing time will be. Fig. 4 shows the finite element model of the automobile TEG system, including the equivalent geometry of the CFD model and four complete TEMs of the thermal-electric numerical model. In the equivalent geometry, the tetrahedral mesh is used due to the irregularity of structure, and all meshes were generated according to their specific physical fields, such as the fined mesh at corners and the boundary layer mesh for the contact surfaces between the solid region and fluid region. In the complete TEM geometry, hexahedron mesh was used because of its regular structure, and all meshes were generated by a sweeping method. It is

necessary to choose a reasonable grid size to make a tradeoff between model accuracy and computing time.

In this work, steady-state numerical calculations of the transient CFD model and the transient thermal-electric numerical model are carried out to check the grid independence. The average exhaust temperature of 615.46 K and average exhaust mass flow rate of 18.26 g/s under the complete HWFET driving cycle are used as steady-state exhaust inlet boundary conditions. Other boundary conditions were the same as those in transient numerical calculation. All numerical calculations were performed in a workstation with 8 cores and 64 G storage. The hot-side temperature of TEM1 and output voltage of four TEMs were taken as the basis for selecting a reasonable grid system of the abovementioned models. As listed in Table 4, the steady-state results of the CFD model and the thermal-electric numerical model under four grid systems are given. Taking the case with the largest number of grids as the baseline, the corresponding error was calculated. The time required for transient numerical calculation is about 765 times longer than that of steady-state numerical calculation for a complete HWFET driving cycle. Therefore, to shorten the computing time and maintain the model accuracy, a grid system with 751672 grids was selected to conduct transient numerical calculation of the transient CFD model. Taking the corresponding steady-state temperature as the boundary conditions of the thermal-electric numerical model, the output performance of TEMs under four grid systems was obtained. Compared with the CFD model, the computing time of the thermal-electric numerical model is much less. Similarly, the grid system with 50619 grids was selected to carry out the transient numerical calculation of the transient thermal-electric numerical model.

Table 4. Grid analysis of the hybrid transient CFD-thermoelectric numerical model

Steady-state results of the CFD model			
grid number	computing time	hot-side temperature of TEM1	error of temperature
2952180	12h16min	506.52 K	0
1268538	6h48min	506.79 K	0.053%
751672	4h30min	506.92 K	0.079%
347888	2h16min	507.31 K	0.156%
Steady-state results of the thermal-electric numerical model			
grid number	computing time	output voltage of four TEMs	error of output voltage
99840	34min	12.651 V	0
57885	20min	12.654 V	0.024%
50619	17min	12.655 V	0.032%
46523	12min	12.659 V	0.063%

2.6 Model validation

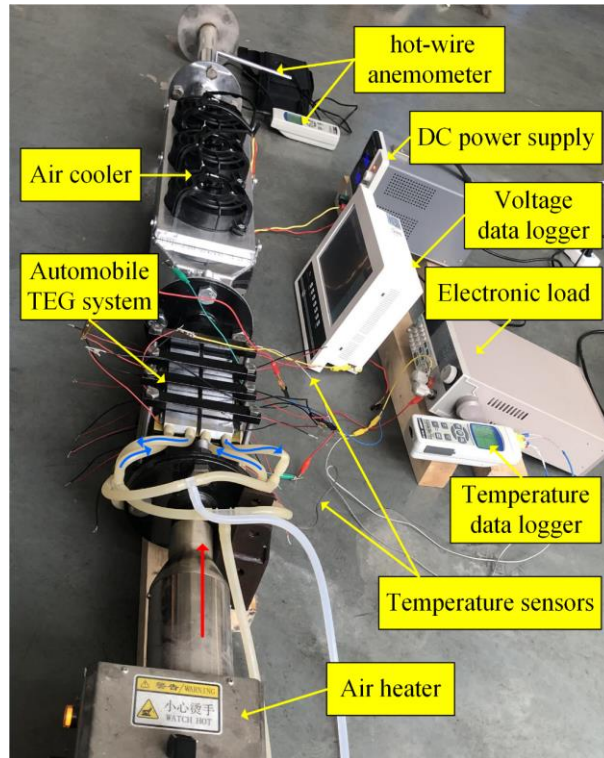


Fig. 5. Transient experiments of the automobile TEG system.

To verify the accuracy of the hybrid transient CFD-thermoelectric numerical model, transient experiments for the automobile TEG system were performed. Fig. 5 shows the designed transient performance test bench. An air heater (F1-R1055, FTV, China) was used to provide a heat source for the automobile TEG system. The air temperature and air velocity can be adjusted instantaneously by the knob on the air heater. The maximum power of the air heater is 5 kW. The tap water with a constant temperature of 284.85 K and a constant flow rate of 21.19 g/s flows through heat sinks of the automobile TEG system to dissipate the heat of TEMs. Two K-type temperature sensors (WRNT, Huarun, China) were installed at the inlet and outlet of the automobile TEG system to measure the air temperatures. The air temperatures were read and recorded by a temperature data logger (RDXL4SD, OMEGA, US) with an accuracy of $\pm 0.4\%$. To test the output performance of the automobile TEG system in the load circuit, an electronic load (IT8500+, ITECH, China) was connected in series with the four TEMs in the same row. The load resistance was set to 17 Ω . As the electronic load can not record the transient output voltage, a voltage data logger (KSF, Keshun, China), with an accuracy of 0.2%, was used. To record the transient air velocity, a hot-wire anemometer (HHF-SD1, OMEGA, US) with an accuracy of $\pm 5\%$, was installed on the pipe behind the automobile TEG system. The operating temperature of the hot-wire anemometer shall not exceed 50°C. Therefore, an air cooler was installed between the automobile TEG system and the hot-wire anemometer, which was powered by a

DC power supply (UTP1305, UNI-T, China). The sampling time of the temperature data logger, voltage data logger, and hot-wire anemometer can be set as 1 s, 2 s, 5 s, 10 s, etc. To obtain more accurate test results, a minimum sampling time of 1 s was adopted.

During transient experiments, the transient air temperature and velocity were obtained, which were taken as the transient inlet boundary conditions of the air in the transient CFD model. However, there is a large temperature drop from the inlet to the outlet of the air cooler, resulting in the error between the measured air velocity and the actual one, which is affected by the temperature dependence of air density. To eliminate this error, the inlet air velocity is modified by $v_{in} = \frac{\rho_{air}(T_{test}) \times v_{test} \times A_{test}}{\rho_{air}(T_{in}) \times A_{in}}$. Furthermore, the transient average temperatures on both ends of the TEMs obtained from the transient CFD model were used as the transient temperature boundary conditions of the transient thermal-electric numerical model. Ultimately, the transient output performance of the automobile TEG system was predicted. Fig. 6 shows the comparison of transient output voltage between experimental and model results. The predicted output voltage enables a greater delay in response than the experimental voltage, which can be attributed to the signal delay of the sensors. When the air temperature changes instantaneously, the temperature sensors will not respond immediately due to the thermal inertia. The average error of transient output voltage between experimental and model results is 6.43%. Due to the measurement error of instruments and the neglect of thermal grease in the numerical model, this tiny error is acceptable for transient experiments.

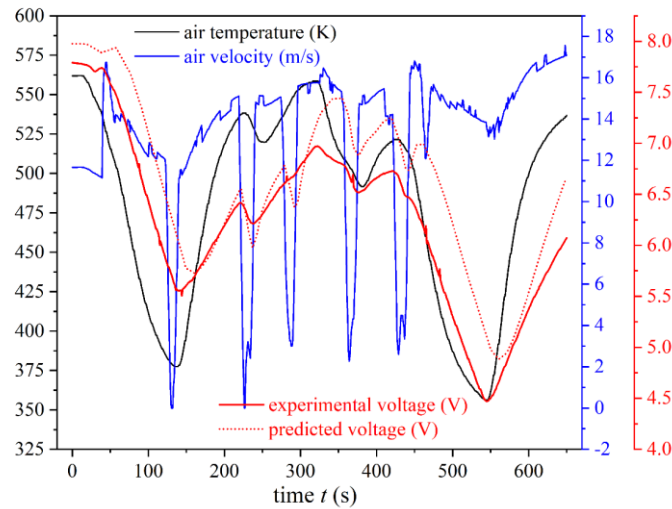


Fig. 6. Comparison of the transient output voltage of the automobile TEG system between experimental results and model results.

3. Results and discussion

3.1 Physical field distribution characteristics of the automobile thermoelectric generator system

CFD model is widely used to analyze the thermodynamic performance of automobile TEG systems. Considering the time dependence of exhaust temperature and mass flow rate, the transient CFD model is used to study the dynamic performance of the automobile TEG system under a complete HWFET driving cycle. Fig. 7 shows the physical field distribution of the automobile TEG system at $t = 100$ s, 300 s, 500 s, and 700 s obtained by the transient CFD model. At $t = 100$ s, 300 s, 500 s, and 700 s, the exhaust temperatures are 614.48 K, 598.96 K, 620.29 K, and 620.89 K, respectively, and the exhaust mass flow rates are 22.54 g/s, 33.30 g/s, 18.18 g/s, and 27.01 g/s, respectively. In general, the hot-side temperature of the heat exchanger increases with the increase of exhaust temperature and mass flow rate, and the influence of exhaust temperature is more obvious than that of exhaust mass flow rate. According to the temperature distribution of the equivalent automobile TEG system (see Fig. 7(a)), the hot-side temperature of the heat exchanger is the highest at $t = 500$ s, followed by those of $t = 700$ s, $t = 100$ s, and $t = 300$ s. Although the exhaust mass flow rate at $t = 500$ s is lower than that at $t = 700$ s, and the exhaust temperature is almost the same, the hot-side temperature of the heat exchanger at $t = 500$ s is higher. This can be attributed to thermal inertia, that is, the exhaust temperature drops from a higher level before the time point of $t = 500$ s, and rises from a lower level before $t = 700$ s, as can be found in Fig. 2. A similar phenomenon between $t = 100$ s and $t = 300$ s can also be explained by this reason.

Fig. 7(b) shows the velocity distribution on the selected cross-sections. The fluid velocity of exhaust gas is directly dependent on the exhaust mass flow rate. Therefore, the fluid velocity of exhaust gas at $t = 300$ s is the highest, followed by those of $t = 700$ s, $t = 100$ s, and $t = 500$ s. Besides, the closer to the center of the exhaust channel is, the greater the fluid velocity of exhaust gas is.

Fig. 7(c) shows the temperature distribution on the hot-side surface of the equivalent TEMs. Similarly, the cold-side temperature distribution can be obtained. By extracting average surface values, the transient average temperature on the hot side of the equivalent TEMs $T_{h_TEMi}(t)$ and that on the cold side $T_{c_TEMi}(t)$ are used as temperature boundary conditions of the transient thermal-electric numerical model with which, the output performance of TEMs can be predicted. Also, the overall hot-side temperature of the four TEMs at $t = 500$ s is the highest, which presents the same trend as that of Fig. 7(a). As the exhaust gas flows downward, the exhaust temperature decreases accordingly, resulting in the decrease of hot-side temperature from TEM1 to TEM4. Consequently, the outputs of TEMs located at different positions are various, with TEM1 showing the highest output performance. As the four TEMs are connected in series, the overall output current is limited by the smallest output current among

the TEMs. Therefore, it is necessary to compare the output performance of different TEMs.

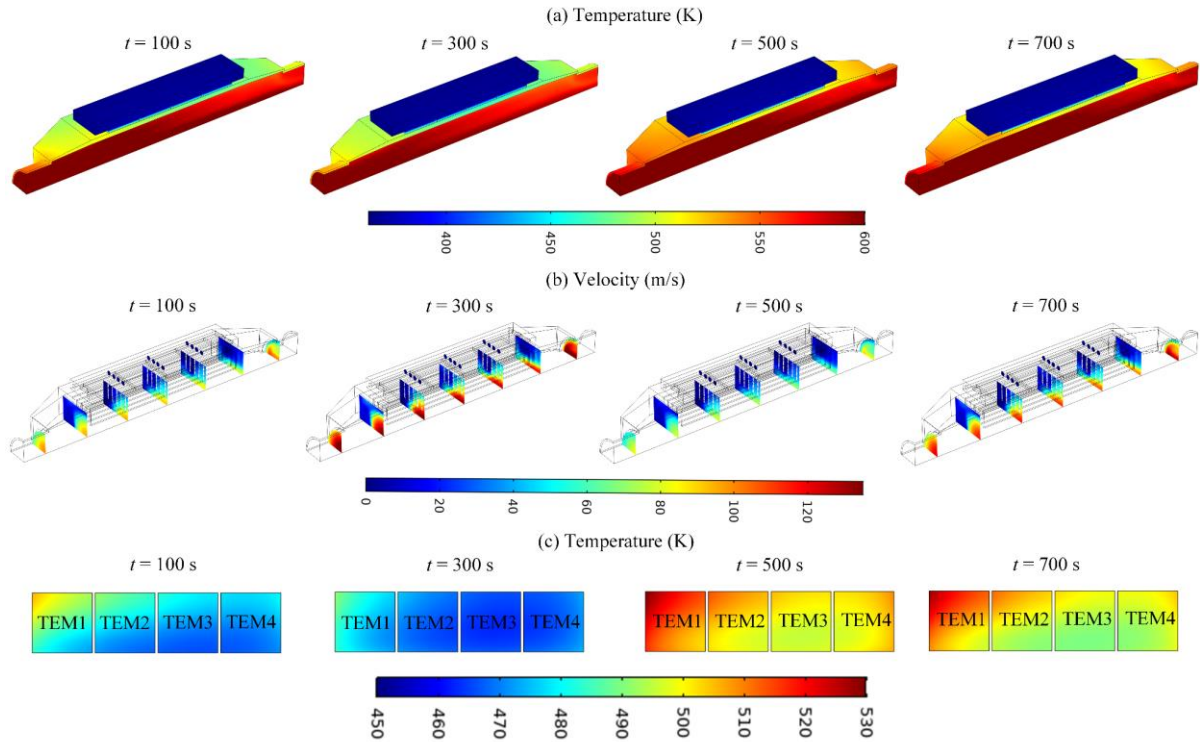


Fig. 7. Physical field distribution characteristics of the automobile TEG system at $t = 100$ s, 300 s, 500 s, and 700 s obtained by the transient CFD model. (a) Temperature distributions of the automobile TEG system. (b) Velocity distributions on the selected cross sections. (c) Temperature distributions of the equivalent TEMs.

3.2 Physical field distribution characteristics of thermoelectric modules

Combined with the temperature boundary conditions obtained by the transient CFD model, the physical field distribution of the complete TEMs is obtained by the transient thermal-electric numerical model, as shown in Fig. 8. Fig. 8(a) shows the temperature distributions of the complete TEMs. There is a large temperature drop in thermoelectric legs because the thermal conductivity of thermoelectric materials is lower than that of copper and ceramic. The lower the thermal conductivity of thermoelectric materials and the greater the temperature difference on both ends of thermoelectric legs are, the better the output performance is. Besides, the load resistance exhibits the highest temperature due to the effect of Joule heat. The temperature profile over time coincides well with the results presented in Fig. 7.

Fig. 8(b) shows the voltage distributions of the complete TEMs. The output voltages of the four TEMs at $t = 100$ s, 300 s, 500 s, and 700 s are 11.03 V, 10.30 V, 13.45 V, and 13.08 V, respectively, which is consistent with the hot-side temperature of the TEMs. This is because the output voltage is proportional to the temperature difference on both sides of the TEMs. Here, the load resistance is 17

Ω and connected with the four TEMs in series. The output power of the automobile TEG system, which is the total output power of the four TEMs, at $t = 100$ s, 300 s, 500 s, and 700 s are 7.15 W, 6.24 W, 10.64 W, and 10.06 W, respectively. The electrical potential increases from negative to positive with the increase of the number of thermoelectric legs in series. It shows that the more thermoelectric legs or TEMs are, the greater the output voltage of the automobile TEG system will be.

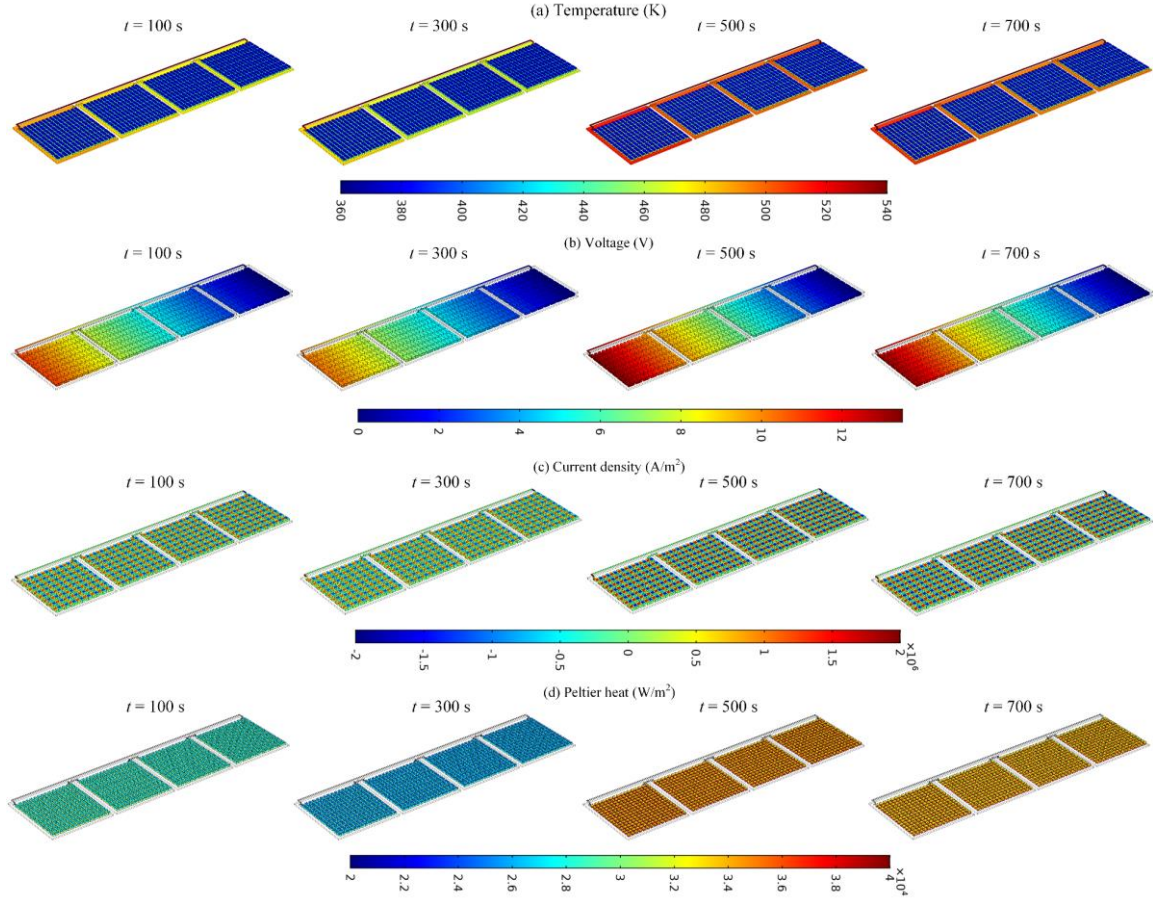


Fig. 8. Physical field distribution characteristics of thermoelectric modules at $t = 100$ s, 300 s, 500 s, and 700 s obtained by the transient thermal-electric numerical model. (a) Temperature distributions of the complete TEMs. (b) Voltage distributions of the complete TEMs. (c) Current density distributions of the complete TEMs. (d) Distributions of $\alpha I_L T$ along with thermoelectric legs.

Fig. 8(c) shows the current density distributions of the complete TEMs. It can be observed that the highest current density occurs in the copper sheets due to the lowest electrical resistivity of copper. The absolute value of the current density of the two adjacent rows of copper sheets is equal, but the direction of the current is opposite. The overall output current can be obtained by multiplying the current density of a selected section by its cross-sectional area.

Driven by the temperature difference, the carriers (electrons in n-type thermoelectric legs and holes in p-type thermoelectric legs) move from the hot side to the cold side. Due to the Peltier effect, carrier

dissipation on the hot side will absorb heat, while carrier accumulation on the cold side will release heat. The hot and cold side Peltier heat can be estimated by $\alpha(T_h)I_L T_h$ and $\alpha(T_c)I_L T_c$, respectively. Fig. 8(d) shows the distribution of $\alpha I_L T$ in thermoelectric legs. Obviously, Peltier heat on the hot side is larger than that on the cold side. This is because the Peltier heat mainly depends on the absolute temperature for the TEMs with the same output current and similar Seebeck coefficient of thermoelectric materials.

3.3 Dynamic response characteristics of the automobile thermoelectric generator system

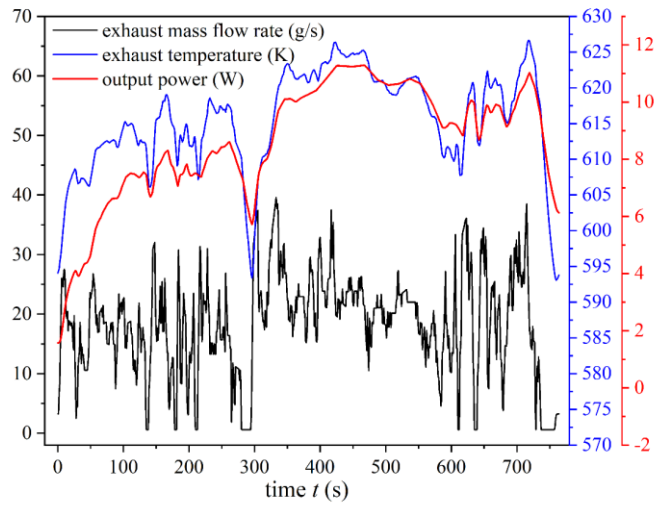


Fig. 9. Dynamic output power of the automobile TEG system under a complete HWFET driving cycle.

With the variation of exhaust temperature and exhaust mass flow rate, the output power of the automobile TEG system fluctuates, as shown in Fig. 9. When the vehicle is under acceleration or deceleration conditions, the fuel consumption will increase or decrease correspondingly. Therefore, the exhaust mass flow rate changes consistently with the vehicle speed and fluctuates greatly. Compared with the rapid changing of exhaust mass flow rate, the transient variation of exhaust temperature is smoother, which is caused by the thermal inertia of the exhaust system. Furthermore, the change of output power of the automobile TEG system is more stable than that of the exhaust temperature. When $260 \text{ s} \leq t \leq 296 \text{ s}$, the exhaust temperature decreases from 647.43 K to 593.16 K and increases from 593.16 K to 623.22 K when $296 \text{ s} \leq t \leq 350 \text{ s}$. The corresponding output power decreases firstly from 8.58 W to 5.72 W and then increases to 10.11 W. In addition, the output power does not respond to the short-term fluctuation of exhaust temperature, as indicated by the profile near $t = 400 \text{ s}$. Due to the rapid changes in exhaust temperature from one level to another, the output power does not have sufficient time to respond before the exhaust temperature returns to the original level.

In the process of heat transfer from the exhaust gas to TEMs, there is a hysteresis in response due to thermal inertia.

Under the complete HWFET driving cycle, the maximum output power of 11.29 W is achieved at $t = 467$ s. It is worth noting that 1/4 structure of the automobile TEG system is used in this paper. Therefore, the maximum output power of the whole automobile TEG system is 45.16 W. The total electrical energy generated within the period of 765 s is 26460 J. However, the electrical energy predicted through the steady-state performance analysis within the period of 765 s is 28830 J. The energy generation predicted by the transient model is 8.96% lower than that expected in the steady-state analysis, which indicates that the steady-state performance analysis may overestimate the output performance of the automobile TEG system under the actual driving conditions. Therefore, it is essential to accurately predict the dynamic performance via a reasonable transient model.

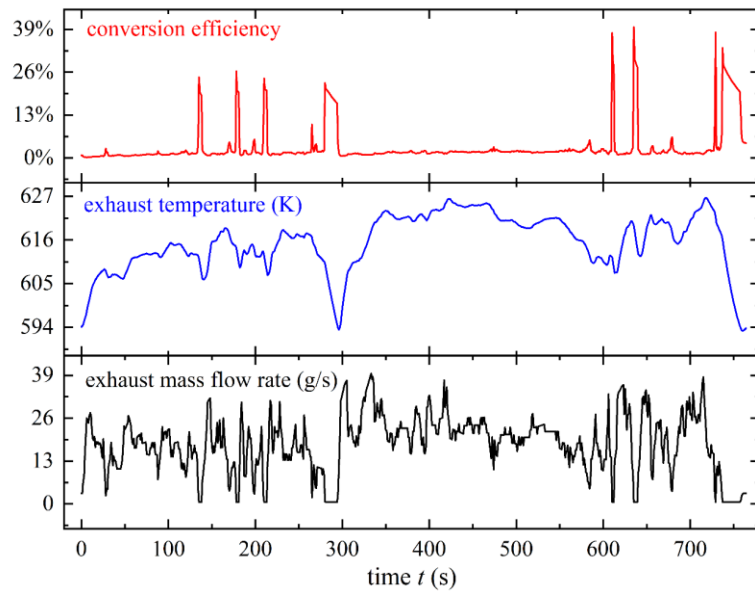


Fig. 10. Dynamic conversion efficiency of the automobile TEG system under a complete HWFET driving cycle.

Fig. 10 shows the dynamic conversion efficiency of the automobile TEG system under a complete HWFET driving cycle. Different from the dynamic output power, the dynamic conversion efficiency fluctuates dramatically. According to Eq. (14), the conversion efficiency is inversely proportional to the exhaust mass flow rate. Therefore, the conversion efficiency increases with the decrease of exhaust mass flow rate, and vice versa. When the exhaust mass flow rate is close to 0, the conversion efficiency reaches the highest value. At $t = 635$ s, a maximum conversion efficiency of 39.68% is achieved, which is obviously higher than the reported values (about 2%) in previous studies. The reason for this is that even though the exhaust mass flow rate is reduced to 0, the hot-side temperature of TEMs remains near the previous state under the effect of thermal inertia. However, the ultrahigh conversion efficiency

is only a transient value, which can not reflect the overall conversion efficiency of the automobile TEG system under a complete driving cycle. Here, the average conversion efficiency predicted by the hybrid transient CFD-thermoelectric numerical model is 3.29% within the period of 765 s, while that predicted by the steady-state model is 1.66%. It seems that the transient fluctuation of the exhaust heat source may amplify the conversion efficiency of the automobile TEG system.

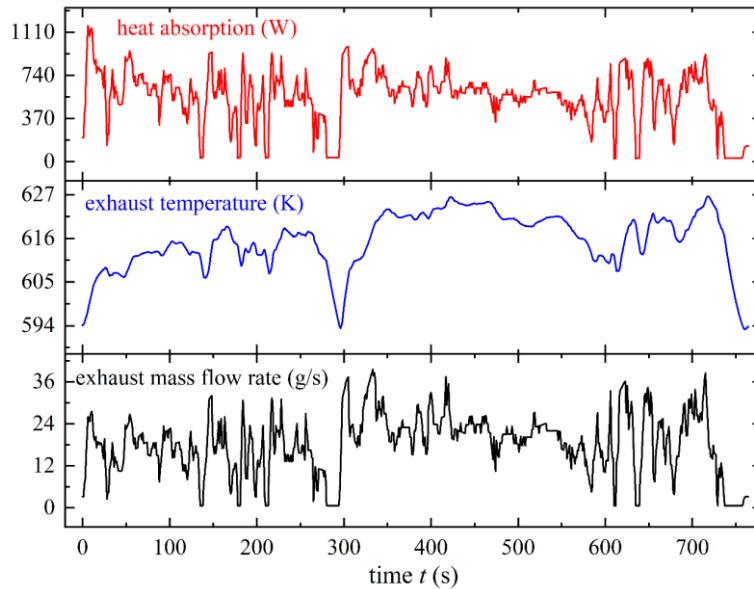


Fig. 11. Dynamic heat absorption of the automobile TEG system under a complete HWFET driving cycle.

Fig. 11 shows the dynamic heat absorption of the automobile TEG system extracted from the exhaust gas under a complete HWFET driving cycle. The changing trend of absorbed heat is completely consistent with that of exhaust mass flow rate because the absorbed heat is directly proportional to the exhaust mass flow rate. However, the amplitude of heat absorbed may be greater or less than that of the exhaust mass flow rate. This is because the temperature drop from the inlet to the outlet of the exhaust gas also affects the heat absorption, and there is a delay in the response of the outlet temperature of the exhaust gas.

3.4 Dynamic response characteristics of thermoelectric modules

According to the CFD results, the dynamic hot-side temperatures of four TEMs are obtained, as shown in Fig. 12. It can be observed that the hot-side temperature of TEM1 is the highest, followed by those of TEM2, TEM4, and TEM3. In general, the hot-side temperature of the TEM decreases as the exhaust gas flows downward. However, the hot-side temperature of TEM4 is higher than that of TEM3, and the hot-side temperature of TEM1 is much higher than that of TEM2. This is because TEM1 and TEM4 extract heat from exhaust gas not only through the heat exchanger area covered by the TEM

but also through the area between the inlet (or outlet) and TEM1 (or TEM4). Besides, the hot-side temperature curve of TEMs is flatter than that of exhaust temperature because of the thermal inertia in the process of heat transfer from the exhaust gas to TEMs. The transient hot-side temperature of TEMs in Fig. 12 is taken as the hot-side temperature boundary condition. Combined with the transient cold-side temperature of TEMs (not shown in the figure) and grounded boundary conditions, the dynamic output performance of TEMs is predicted by the transient thermal-electric numerical model.

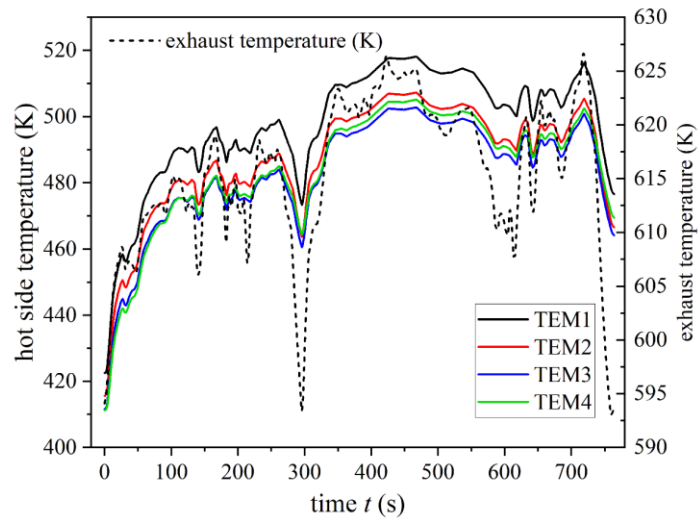


Fig. 12. Dynamic hot-side temperature of thermoelectric modules under a complete HWFET driving cycle.

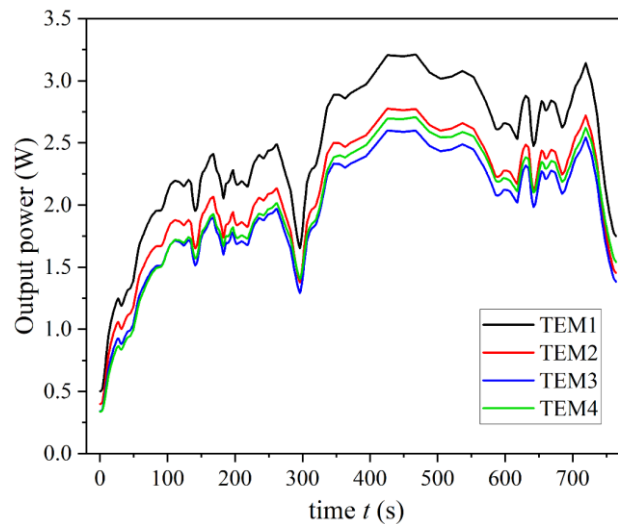


Fig. 13. Dynamic output power of thermoelectric modules under a complete HWFET driving cycle.

Fig. 13 shows the dynamic output power of thermoelectric modules under a complete HWFET driving cycle. Combined with Fig. 10, The conversion efficiency increases when the power generated decreases. The reason is that the heat absorption of the automobile TEG system is significantly decreased when the vehicle speed is close to 0, yet the hot-side temperature will not respond

immediately, and the output power only drops slowly. Combined with Fig. 12, it can be considered that the output power curve is obtained by amplifying the hot-side temperature curve. This is because the output power is proportional to the square of the temperature difference of TEMs, which mainly depends on the hot-side temperature of the TEMs as the cold-side temperature of the TEMs is almost constant. The output power of TEM1 is remarkably higher than that of the other TEMs. When all the TEMs are connected electrically in series or parallel, the parasitic power loss caused by the uneven output of TEMs plays a negative role in the overall output performance of the automobile TEG system. This parasitic power loss can not be neglected when there are a great number of TEMs in the automobile TEG system. In this case, the topological optimization of the TEMs is suggested. Besides, the thermal inertia in the heat transfer process from the hot side to the cold side of the TEM is smaller than that from the exhaust gas to TEMs, and there is no response delay in the electrical parameters. Therefore, the changing trend of output power is consistent with that of hot-side temperature.

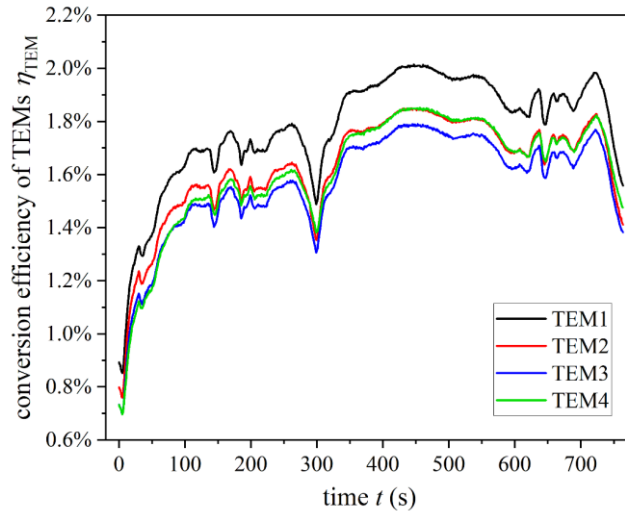


Fig. 14. Dynamic conversion efficiency of thermoelectric modules under a complete HWFET driving cycle.

Different from the conversion efficiency of the automobile TEG system, the conversion efficiency of the TEMs varies more smoothly, as shown in Fig. 14. Here, the conversion efficiency of the TEMs is computed by Eq. (16), and it will not change with the variation of exhaust mass flow rate. Even though the exhaust mass flow rate decreases to 0 at a certain point during the transient state, the TEMs will continue extracting heat from the heat exchanger and converting it into electrical energy. This is because the internal energy in solid regions does not change instantaneously with the exhaust mass flow rate as a result of the thermal inertia effect. The average conversion efficiencies of TEM1, TEM2, TEM3, and TEM4 within the period of 765 s are 1.78%, 1.63%, 1.57%, and 1.61%, respectively. They are lower than that of the automobile TEG system (3.29%), which can be explained by the above

reasons. The conversion efficiency of TEM4 gradually increases, surpassing the conversion efficiency of TEM3 and reaching close to that of TEM2. Similar trends of hot-side temperature and output power can be observed in Fig. 12 and Fig. 13, respectively. The reason for this is that the exhaust mass flow rate reaches a relatively higher level when $t > 300$ s, and this larger exhaust mass flow rate leads to a more intense reverse flow of exhaust gas at the outlet of the heat exchanger, thus, enabling TEM4 to absorb more heat.

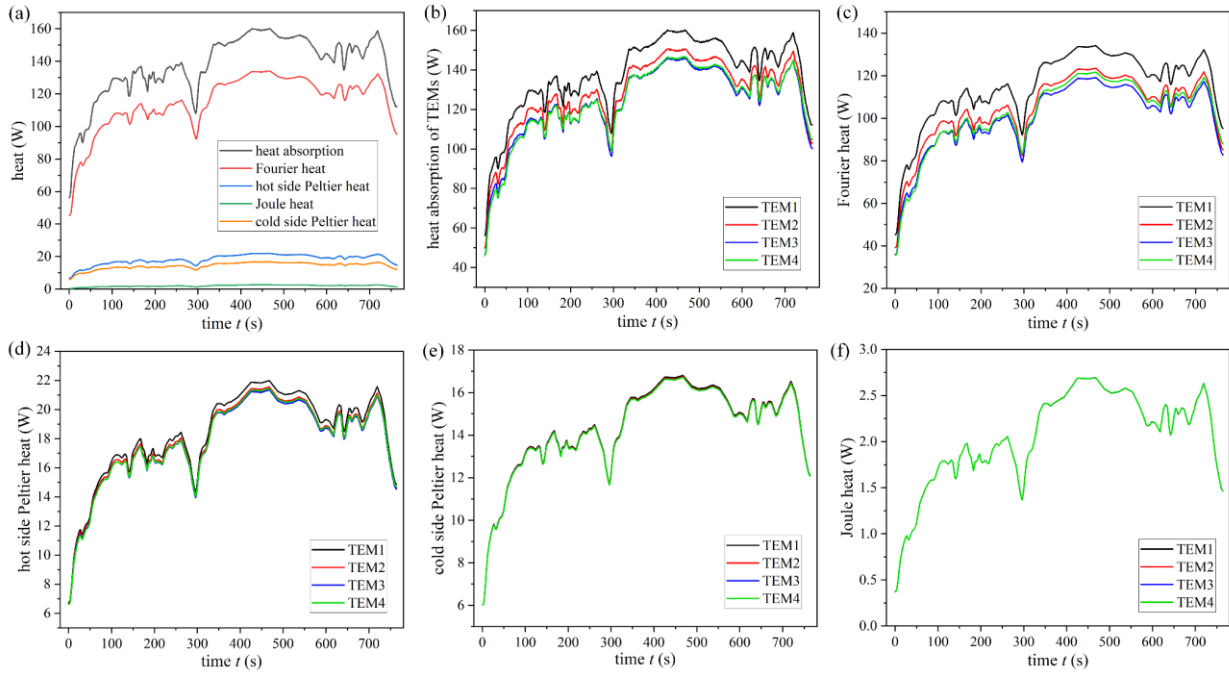


Fig. 15. Transient heat of thermoelectric modules under a complete HWFET driving cycle. (a) Different heat generated in TEM1. (b) Heat absorption of different TEMs. (c) Fourier heat of thermoelectric legs for different TEMs. (d) Hot-side Peltier heat of thermoelectric legs for different TEMs. (e) Cold-side Peltier heat of thermoelectric legs for different TEMs. (f) Joule heat of thermoelectric legs for different TEMs.

Fig. 15 shows the transient heat of the TEMs under a complete HWFET driving cycle. In addition to heat absorbed from the heat exchanger, other forms of heat also occur in the working process of the TEMs, which include Fourier heat along the thermoelectric legs, Peltier heat on both hot and cold sides of thermoelectric legs, and Joule heat within the thermoelectric legs. Fig. 15 (a) shows the amount of these different heat generated in TEM1. In general, the absorbed heat is approximately equal to the hot-side Peltier heat plus Fourier heat and minus half the Joule heat. Fourier heat dominates the heat absorption, while Joule heat only accounts for a small part. For this reason, the changing trend of Fourier heat (see Fig. 15(c)) is consistent with that of absorbed heat (see Fig. 15(b)). Also, the variation of Fourier heat is slightly smoother than that of absorbed heat because of the thermal inertia. Fig. 15(d) and Fig. 15(e) show the hot-side Peltier heat and cold-side Peltier heat of thermoelectric legs for

different TEMs, respectively. The difference of hot-side Peltier heat among different TEMs is greater than that of cold-side Peltier heat because the hot-side temperature of different TEMs is not uniform while the cold-side temperature is almost the same. Fig. 15(f) shows the Joule heat of thermoelectric legs for different TEMs. Here, the four TEMs are connected in series, and their internal resistances are almost the same. Therefore, there is no difference between Joule heat curves of different TEMs.

4. Conclusions

In this paper, a hybrid transient CFD-thermoelectric numerical model is proposed, which considers the transient input of the heat source, temperature dependence, impedance matching, and heat loss. The model is used to predict the transient performance of the automobile TEG system under the actual driving conditions. Firstly, a heavy truck is set to run under HWFET driving conditions, and the obtained transient exhaust temperature and mass flow rate are used as the transient heat source input of the model. Then, the hybrid transient CFD-thermoelectric numerical model of the automobile TEG system is solved by using the finite element simulation of COMSOL. The dynamic output performance of the automobile TEG system, such as dynamic output power and conversion efficiency, is obtained. Finally, a transient test is carried out on the designed test bench to verify the accuracy of the hybrid transient CFD-thermoelectric numerical model. Based on the numerical results, the following conclusions are obtained:

(1) The hybrid transient CFD-thermoelectric numerical model can accurately predict the physical field distribution characteristics of the automobile TEG system under any transient exhaust heat source input, which provides a new tool to evaluate the dynamic performance of automobile TEG systems. The average deviation of transient output voltage between the model and experimental results is 6.43%, which is within the acceptable range.

(2) Under a complete HWFET driving cycle, the output power of the automobile TEG system changes more smoothly than that of exhaust temperature due to the thermal inertia during the heat transfer process from the exhaust gas to TEMs. For the complete geometry of the automobile TEG system, the maximum output power of 45.16 W is achieved, and the total energy generation is 26460 J within the period of 765 s, which is 8.96% lower than that expected in the steady-state performance analysis.

(3) Different from the output power, the conversion efficiency of the automobile TEG system fluctuates greatly because it is inversely proportional to the exhaust mass flow rate. The ultra-high transient conversion efficiency of 39.68% is achieved at $t = 635$ s and the average conversion efficiency

is 3.29% within the period of 765 s, which is significantly higher than the average conversion efficiency of 1.66% observed from steady-state performance analysis.

(4) The dynamic conversion efficiency of the TEM is quite different from that of the automobile TEG system because the TEM does not extract heat directly from the exhaust gas. The output performance of the TEM decreases with the downward flow of exhaust gas, except for the TEM in the last row. Besides, the topological relationship among TEMs plays a negative role in the overall output performance of the automobile TEG system, especially when the automobile system contains a great number of TEMs.

(5) In future works, the hybrid transient CFD-thermoelectric numerical model will be further improved by returning the output of the thermal-electric numerical model to the CFD model until convergence is reached for each step. Also, the influence of the neglected heat on the model accuracy will be further studied.

Acknowledgements

This work was supported by the National Natural Science Foundation of China (52072217 and 22179071), the Major Technological Innovation Project of Hubei Science and Technology Department (2019AAA164), as well as Ningbo Science and Technology Bureau's Technology under Grant No. 2019B10042.

References

- [1] Yang J, Stabler FR. Automotive Applications of Thermoelectric Materials. *J Electron Mater* 2009;38:1245-51.
- [2] Shen Z-G, Tian L-L, Liu X. Automotive exhaust thermoelectric generators: Current status, challenges and future prospects. *Energy Convers Manage* 2019;195:1138-73.
- [3] Brito FP, Pacheco N, Vieira R, Martins J, Martins L, Teixeira J, et al. Efficiency improvement of vehicles using temperature controlled exhaust thermoelectric generators. *Energy Convers Manage* 2020;203:112255.
- [4] Twaha S, Zhu J, Yan Y, Li B. A comprehensive review of thermoelectric technology: Materials, applications, modelling and performance improvement. *Renewable Sustainable Energy Rev* 2016;65:698-726.
- [5] Crane D, LaGrandeur J, Jovovic V, Ranalli M, Adldinger M, Poliquin E, et al. TEG On-Vehicle Performance and Model Validation and What It Means for Further TEG Development. *J Electron*

Mater 2013;42:1582-91.

- [6] Lan S, Yang Z, Chen R, Stobart R. A dynamic model for thermoelectric generator applied to vehicle waste heat recovery. *Appl Energy* 2018;210:327-38.
- [7] Liu X, Deng YD, Li Z, Su CQ. Performance analysis of a waste heat recovery thermoelectric generation system for automotive application. *Energy Convers Manage* 2015;90:121-7.
- [8] Massaguer A, Massaguer E, Comamala M, Pujol T, Montoro L, Cardenas MD, et al. Transient behavior under a normalized driving cycle of an automotive thermoelectric generator. *Appl Energy* 2017;206:1282-96.
- [9] Risseh AE, Nee H-P, Goupil C. Electrical Power Conditioning System for Thermoelectric Waste Heat Recovery in Commercial Vehicles. *IEEE Transactions on Transportation Electrification*. 2018;4:548-62.
- [10] Wan Q, Liu X, Gu B, Bai W, Su C, Deng Y. Thermal and acoustic performance of an integrated automotive thermoelectric generation system. *Appl Therm Eng* 2019;158:113802.
- [11] He W, Guo R, Liu S, Zhu K, Wang S. Temperature gradient characteristics and effect on optimal thermoelectric performance in exhaust power-generation systems. *Appl Energy* 2020;261:114366.
- [12] Chen W-H, Lin Y-X, Chiou Y-B, Lin Y-L, Wang X-D. A computational fluid dynamics (CFD) approach of thermoelectric generator (TEG) for power generation. *Appl Therm Eng* 2020;173:115203.
- [13] Luo D, Wang R, Yu W. Comparison and parametric study of two theoretical modeling approaches based on an air-to-water thermoelectric generator system. *J Power Sources* 2019;439:227069.
- [14] Hu X, Takazawa H, Nagase K, Ohta M, Yamamoto A. Three-Dimensional Finite-Element Simulation for a Thermoelectric Generator Module. *J Electron Mater* 2015;44:3637-45.
- [15] Shadmehri M, Narei H, Ghasempour R, Shafii MB. Numerical simulation of a concentrating photovoltaic-thermal solar system combined with thermoelectric modules by coupling Finite Volume and Monte Carlo Ray-Tracing methods. *Energy Convers Manage* 2018;172:343-56.
- [16] Fernández-Yañez P, Armas O, Capetillo A, Martínez-Martínez S. Thermal analysis of a thermoelectric generator for light-duty diesel engines. *Appl Energy* 2018;226:690-702.
- [17] Meng J-H, Zhang X-X, Wang X-D. Characteristics analysis and parametric study of a thermoelectric generator by considering variable material properties and heat losses. *Int J Heat Mass Transfer* 2015;80:227-35.
- [18] Yan S-R, Moria H, Asaadi S, Sadighi Dizaji H, Khalilarya S, Jermisittiparsert K. Performance and

-
- profit analysis of thermoelectric power generators mounted on channels with different cross-sectional shapes. *Appl Therm Eng* 2020;115455.
- [19] Hsiao YY, Chang WC, Chen SL. A mathematic model of thermoelectric module with applications on waste heat recovery from automobile engine. *Energy*. 2010;35:1447-54.
- [20] Luo D, Wang R, Yu W, Sun Z, Meng X. Modelling and simulation study of a converging thermoelectric generator for engine waste heat recovery. *Appl Therm Eng* 2019;153:837-47.
- [21] Catalan L, Araiz M, Aranguren P, Astrain D. Computational study of geothermal thermoelectric generators with phase change heat exchangers. *Energy Convers Manage* 2020;221:113120.
- [22] Weng C-C, Huang M-J. A simulation study of automotive waste heat recovery using a thermoelectric power generator. *Int J Therm Sci* 2013;71:302-9.
- [23] Kempf N, Zhang Y. Design and optimization of automotive thermoelectric generators for maximum fuel efficiency improvement. *Energy Convers Manage* 2016;121:224-31.
- [24] Zhang Y. Thermoelectric Advances to Capture Waste Heat in Automobiles. *ACS Energy Letters*. 2018;3:1523-4.
- [25] Jia X-D, Wang Y-J, Gao Y-W. Numerical simulation of thermoelectric performance of linear-shaped thermoelectric generators under transient heat supply. *Energy*. 2017;130:276-85.
- [26] Reddy BVK, Barry M, Li J, Chyu MK. Mathematical modeling and numerical characterization of composite thermoelectric devices. *Int J Therm Sci* 2013;67:53-63.
- [27] Luo D, Yan Y, Wang R, Zhou W. Numerical investigation on the dynamic response characteristics of a thermoelectric generator module under transient temperature excitations. *Renewable Energy* 2021;170:811-23.
- [28] Ma T, Lu X, Pandit J, Ekkad SV, Huxtable ST, Deshpande S, et al. Numerical study on thermoelectric–hydraulic performance of a thermoelectric power generator with a plate-fin heat exchanger with longitudinal vortex generators. *Appl Energy* 2017;185:1343-54.
- [29] Li W, Peng J, Xiao W, Wang H, Zeng J, Xie J, et al. The temperature distribution and electrical performance of fluid heat exchanger-based thermoelectric generator. *Appl Therm Eng* 2017;118:742-7.
- [30] Luo D, Wang R, Yu W, Zhou W. A novel optimization method for thermoelectric module used in waste heat recovery. *Energy Convers Manage* 2020;209:112645.
- [31] Luo D, Wang R, Yu W, Zhou W. A numerical study on the performance of a converging thermoelectric generator system used for waste heat recovery. *Appl Energy* 2020;270:115181.
- [32] Massaguer A, Massaguer E, Comamala M, Pujol T, González JR, Cardenas MD, et al. A method

-
- to assess the fuel economy of automotive thermoelectric generators. *Appl Energy* 2018;222:42-58.
- [33] Gou X, Yang S, Xiao H, Ou Q. A dynamic model for thermoelectric generator applied in waste heat recovery. *Energy*. 2013;52:201-9.
- [34] Nithyanandam K, Mahajan RL. Evaluation of metal foam based thermoelectric generators for automobile waste heat recovery. *Int J Heat Mass Transfer* 2018;122:877-83.
- [35] Chen W-H, Liao C-Y, Hung C-I. A numerical study on the performance of miniature thermoelectric cooler affected by Thomson effect. *Appl Energy* 2012;89:464-73.
- [36] Luo D, Wang R, Yu W, Zhou W. Parametric study of a thermoelectric module used for both power generation and cooling. *Renewable Energy* 2020;154:542-52.
- [37] Shi Y, Chen X, Deng Y, Gao H, Zhu Z, Ma G, et al. Design and performance of compact thermoelectric generators based on the extended three-dimensional thermal contact interface. *Energy Convers Manage* 2015;106:110-7.
- [38] Massaguer A, Pujol T, Comamala M, Massaguer E. Feasibility study on a vehicular thermoelectric generator coupled to an exhaust gas heater to improve aftertreatment's efficiency in cold-starts. *Appl Therm Eng* 2020;167:114702.
- [39] Sandoz-Rosado E, Stevens R. Robust Finite Element Model for the Design of Thermoelectric Modules. *J Electron Mater* 2010;39:1848-55.
- [40] Anderson JD, Wendt J. *Computational fluid dynamics*: Springer; 1995.
- [41] Fluent A. *Fluent 14.0 user's guide*2011.
- [42] Lv H, Wang X-D, Meng J-H, Wang T-H, Yan W-M. Enhancement of maximum temperature drop across thermoelectric cooler through two-stage design and transient supercooling effect. *Appl Energy* 2016;175:285-92.
- [43] Shittu S, Li G, Xuan Q, Zhao X, Ma X, Cui Y. Electrical and mechanical analysis of a segmented solar thermoelectric generator under non-uniform heat flux. *Energy*. 2020;199:117433.
- [44] Wipke KB, Cuddy MR, Burch SD. ADVISOR 2.1: a user-friendly advanced powertrain simulation using a combined backward/forward approach. *IEEE Trans Veh Technol* 1999;48:1751-61.